Title

Method for improving the spatial resolution of narrow x-ray beam-based x-ray luminescence computed tomography imaging.

Journal

Journal of biomedical optics, 24(8)

ISSN

1083-3668

Authors

Zhang, Yueming
Lun, Michael C
Li, Changqing
et al.

Publication Date

2019-08-01

DOI

10.1117/1.jbo.24.8.086002

Peer reviewed

A method for improving the spatial resolution of narrow x-ray beam based x-ray luminescence computed tomography (XLCT) imaging

YUEMING ZHANG,[1,#] MICHAEL C. LUN,[2,#] CHANGQING LI,[2,*] AND ZHONGXING ZHOU [1,3,4,*]

[1] *School of Precision Instrument and Optoelectronics Engineering, Tianjin University, Tianjin 300072, China*

[2] *Department of Bioengineering, University of California, Merced, Merced, CA, USA*

[3] *Tianjin Key Laboratory of Biomedical Detecting Techniques and Instruments, Tianjin 300072, China*

[4] *Tianjin Shareshine Technology Development Co, Ltd. Tianjin, People's Republic of China*

[#] *These authors contributed to this work equally.*

* cli32@ucmerced.edu * zhouzhongxing@tju.edu.cn

Abstract: X-ray luminescence computed tomography (XLCT) is an emerging hybrid imaging modality which has the potentials for achieving both high sensitivity and spatial resolution simultaneously. However, its high spatial resolution capacity, which is believed to be limited by the aperture size in the case of the narrow x-ray beam based XLCT imaging, has not been fully implemented yet. Herein, we proposed a new scanning strategy, which is achieved by reducing the scanning step size to be less than the x-ray beam size, to break the spatial resolution limit of the traditional narrow x-ray beam based XLCT system. Both numerical simulations and phantom experiments demonstrated that the proposed scanning method greatly improved the reconstruction quality compared with the conventional scanning approach. In the numerical simulations, we scanned a cylindrical object containing 6 embedded targets with the target size or the edge-to-edge distance between targets less than the beam width. With measurements from 6 angular projections, the reconstruction quality of all 6 targets was improved monotonically with reducing scanning step size. The simulation experiments

demonstrated that the proposed scanning method can achieve better results than the traditional one in terms of the dice similarity coefficient, target size error, spatial resolution index and the normalized mean square error. Lastly, we have performed phantom experiments to further demonstrate the efficacy of the proposed method in improving the spatial resolution of XLCT imaging.

Index Terms—reconstruction algorithm, tomographic imaging, x-ray luminescence

I. INTRODUCTION

X-ray luminescence computed tomography (XLCT) is an emerging hybrid molecular imaging modality with promising potentials to have both the high molecular sensitivity of optical imaging and the good spatial resolution of x-ray imaging, which cannot be achieved by either modality alone. Since Pratx *et al.* reported for the first time that narrow-beam selective excitation based XLCT imaging could image the distribution of phosphor particles [1-3], various institutions have made many attempts to further develop and improve XLCT imaging by developing new imaging systems [1, 4-12], building robust reconstruction algorithms [13-15], and designing efficient imaging probes [16-20].

Currently, there are two primary types of scanning modes for XLCT imaging. One is the cone beam based XLCT imaging [9, 21, 22], in which a conical x-ray beam is used to cover the whole object so that the scanning time is as short as a few seconds. The disadvantage of this approach is that the spatial resolution is compromised because the x-ray beam size is larger and cannot be used an anatomical guidance in the image reconstruction. Another scanning mode is the narrow beam based XLCT imaging, in which a collimated or focused x-ray beam is used to scan an object sequentially [1, 11,

12]. The narrow beam based XLCT imaging can have spatial resolution up to a fraction of millimeter because the fine beam size can be applied as anatomical guidance in the XLCT reconstruction algorithm [23]. The disadvantage is its relatively long scanning time due to the small excitation region, although this can be addressed by using a higher sensitivity optical detector [10, 12].

In the traditional narrow x-ray beam based XLCT system design, the fundamental limit of spatial resolution is determined by the beam aperture size [3]. From these reports, we know that it is impossible to separate two targets when the x-ray beam size is larger than the target diameter as well as the target edge-to-edge distance (EED). Zhang *et al.* have reported that the spatial resolution of a narrow beam based XLCT imaging is double the size of the scanning beam diameter [11]. Thus, current efforts to improve the spatial resolution focus on how to obtain a small x-ray beam. There are several approaches to reduce the x-ray beam size. One approach is to focus an x-ray beam with an x-ray optics lens to a fine focal spot. Cong *et al.* proposed a dual cone scanning method with a polycapillary lens, in which the x-ray beam was focused into a spot with a diameter of less than 50 μm [10]. Later, Zhang *et al.* have built a focused x-ray beam based XLCT imaging system with a focused beam size of 150 μm [10]. This method can maximize the intensity of the x-ray energy at the focal point of a dual cone beam. However, the poly-capillary lens is expensive and has a drawback that it is very difficult to focus high-energy x-ray photons. The adoption of low energy x-ray beams (e.g. within the range from 15 keV to 20 keV) would reduce the x-ray penetration ability, and thus, large objects could be difficult or impossible to image. Another approach is to collimate a conical x-ray beam into a fine pencil beam with a small aperture size [11]. The advantage of this approach is

that it is straightforward to be implemented at a very low cost. However, most x-ray photons are absorbed by the collimator leading to a low x-ray utilization efficiency, which contributes to the long measurement time.

In this paper, we have reported an approach to improve the spatial resolution of the narrow beam based XLCT imaging further to break its current spatial resolution limit of double the x-ray beam size. Our approach does not need to add any physical cost, but is accomplished by simply reducing the x-ray beam scanning step sizes. Of course, more scan steps are then needed which results in a longer scanning time. However, this issue can be addressed easily by using a sensitive photon detector and by applying a continuous scanning mode [10]. The efficacy of small scanning step sizes in improving the XCLT imaging quality have been validated by numerical simulations and phantom experiments in this study.

This paper is organized as follows. In Section 2, we have described the XLCT imaging system, the physical and numerical phantom geometry, the XLCT scanning scheme, and the image quality evaluation criteria. In Section 3, we have analyzed the reconstructed XLCT images with different scanning schemes. Lastly, we conclude the paper with some discussions and future directions.

II. METHODS

A. XLCT imaging system

We have performed XLCT imaging of a cylindrical phantom using our focused x-ray beam based XLCT imaging system that was previously described in [10]. Figure 1 below shows a schematic of the XLCT system. In short, we used an x-ray tube (Max: 50 kVp and 1.0 mA) with an attached polycapillary lens (X-Beam Powerflux (Mo Anode), XOS) to generate an x-ray beam that was focused to a fine spot of 100 μm diameter. The object

stage where the phantom is placed was at the focal spot of the x-ray beam and was mounted to a manual lab jack (LJ750/M, Thorlabs) which allows us to adjust the scanning depth (defined as the distance from the object top surface to the scanned section). Based on the phantom's size and location, the x-ray beam diameter varied from approximately 100 to 200 μm. The jack was mounted on a rotational stage (B4872TS-ZR, Velmex Inc.) and then on a linear stage (Unislide MA40, Velmex Inc.) for rotating and translating the object at different depths. The transmitted x-ray beam was detected by an x-ray detector (Shad-o-Box 1024, Teledyne Rad-icon Imag. Corp.) mounted opposite of the x-ray tube and was used to monitor the x-ray beam location relative to the phantom geometry. A single optical fiber bundle was mounted using a custom 3D printed holder and detected the optical photons that reached the object surface close to the fiber bundle and delivered the photons to a fan-cooled photomultiplier tube (PMT) (H7422P-50, Hamamatsu) operated at a control voltage of 0.751 V. The signal from the PMT was then sent to an amplifier (SR445A, Stanford Research Systems) and was amplified 25 times before being filtered with a low-pass filter (BLP-10.7+, Cutoff frequency: 11 MHz, Mini-circuits) to reduce high-frequency noise before finally being collected and displayed by a high-speed oscilloscope (MDO-3014, Tektronix). Finally, the digitized signals acquired by the oscilloscope were saved to a lab computer. The entire system up to the PMT was inside of a light-tight and x-ray shielding lead cabinet with the PMT further shielded from scattered x-ray photons by a lead sheet. The XLCT imaging system was controlled with custom programs on the lab computer.

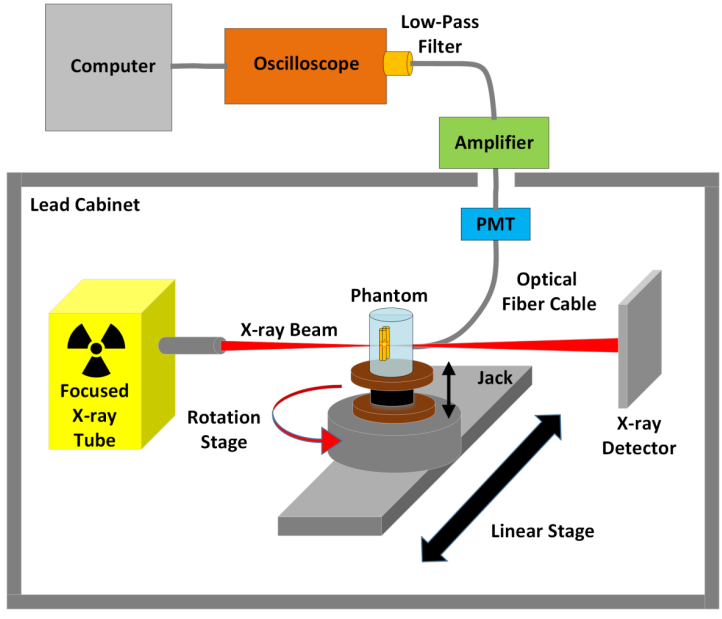

Fig. 1. Schematic of XLCT system used in phantom experiments.

B. Scanning scheme

In the scanning scheme of the conventional narrow x-ray beam based XLCT, the object is scanned by a sequence of single x-ray beams moving at predefined directions and positions, which is similar to the first generation x-ray computed tomography (CT) scanning mode. It can be extended to the multi-beam scanning strategy using multiple pinhole collimators [8], but the scanning step size is still kept equal to the x-ray beam width. Under such kind of scanning strategies, the spatial resolution in narrow beam XLCT is determined by the beam width. In this study, we modified the scanning scheme of the conventional narrow-beam XLCT by reducing the scanning step size to be less than the x-ray beam size. This modification can be performed on both single-beam and multi-beam scanning strategy. Figure 2 shows the single-beam scanning strategy for a typical angular projection. From Fig. 2, the linear scan step size as well as target diameter is set smaller than beam width. For each angular projection, the number of linear scanning

steps (N_l) is determined by the diameter of entire scanning region (D_{reg}) and the scanning step size (S_{step}) as $N_l = D_{reg} / S_{step}$.

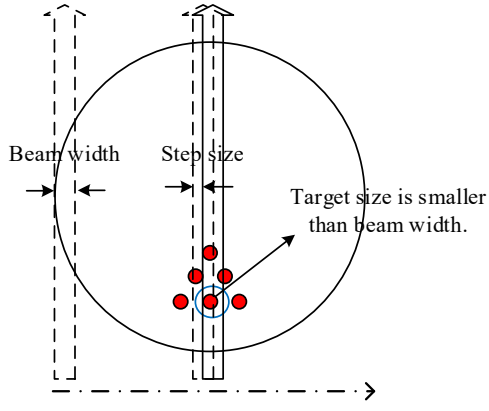

Fig. 2. Schematic of linear scan setup for one typical angular projection. The red dots indicate the targets. The vertical arrows indicate the x-ray beams.

C. Numerical simulation setup

To validate the feasibility and effectiveness of our proposed scanning strategy in XLCT, four cylindrical phantoms (Phantoms A, B, C and D) were designed for numerical simulations. For all phantoms, the diameter and height were set to be 12.8 mm and 10 mm, respectively, as shown in Fig. 3(a). Six luminescent $GOS:Eu^{3+}$ targets of 6 mm in height were placed in the phantoms at a depth of 2 mm. The diameter and edge-to-edge distance (EED) settings of the six targets for all four numerical phantoms are listed in Table I. The positions of the six targets and the four fiber bundles are shown in Fig. 3(b). The targets' diameter is the same as the EED, which has been changed from 0.4 mm to 0.8 mm in this study. In the transverse plot as shown in Fig. 3(b), the six targets were formed an equilateral triangle whose centroid was fixed at (0, -D/4) where D is the background phantom diameter. The absorption coefficient (μ_a) and the reduced scattering coefficient (μ_s`) of the phantom were set to be $0.0072mm^{-1}$ and $0.72mm^{-1}$ at the wavelength of

703 nm, which is the longest wavelength peak in the emission spectrum of $GOS:Eu^{3+}$. In the simulation studies, we set the phosphor particle concentration to be 1.0 and 0 mg/mL in the target and background regions respectively.

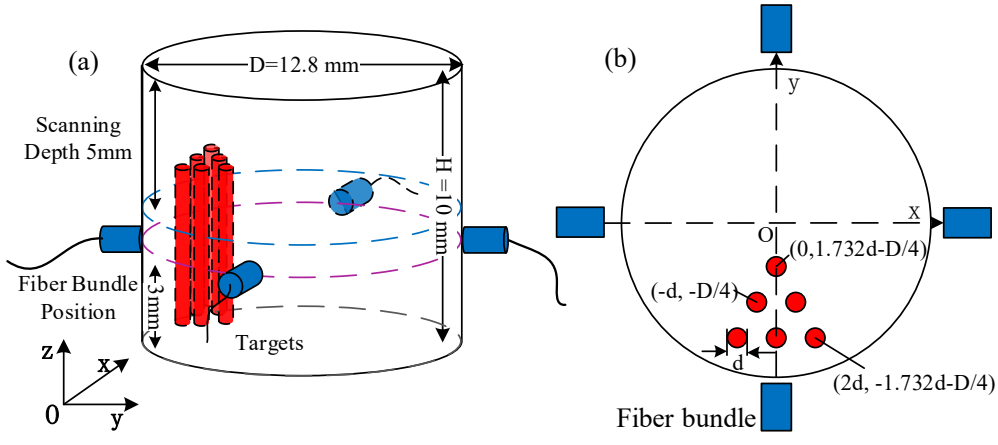

Fig. 3. Phantom geometry and detectors set-up used in the numerical simulations. (a) Overall phantom geometry; (b) Transverse plot of the phantom to show the positions of six targets and four fiber bundles.

Table I.
THE GEOMETRY OF THE TARGETS EMBEDDED IN PHANTOMS A, B, C AND D.

Phantom	A	B	C	D
Target diameter(mm)	0.8	0.6	0.5	0.4
EED(mm)	0.8	0.6	0.5	0.4

For all numerical simulations, four optical fiber bundles were placed 2 mm below the scanned section and 90 degrees apart from each other, which were employed to collect the emitted photons on the phantom surface, as shown in Fig. 3(a). The diameter of the x-ray beam was fixed at 0.8 mm, and the linear scan step size was set to 0.8 mm, 0.4 mm, 0.2 mm and 0.1 mm, respectively, for each simulation. We used 6 angular projections with the angular step size of 30 degrees. The numerical measurements at each angular

projection were generated with the forward model of XLCT proposed in reference [8, 10]. To make the simulations more realistic, 50% white Gaussian noise was added to the numerical measurements.

D. Phantom experimental setup

We performed our XLCT scan on a cylindrical phantom (Figs. 4 and 5). A schematic of the phantom is shown below in Fig. 4(a, b) from which we can see the phantom had a diameter of 25 mm and a height of 40 mm and was composed of 1% intralipid and 2% agar and was embedded off-center with 4 capillary tube targets. The same background solution was mixed with 10 mg/mL of GOS:Eu^{3+} particles (UKL63/UF-R1, Phosphor Tech. Ltd.) and was injected into the capillary tubes (Drummond Scientific) which had an inner diameter (I.D.) and outer diameter (O.D.) of 0.4 and 0.8 mm respectively. After the phantom was created and completely solidified, we performed a microCT scan using our lab-made microCT system previously described in [28] to determine the positions of the embedded targets. A single-slice from the microCT reconstruction, corresponding to the XLCT scanning section, is shown in Fig. 4(c). Based on the image, the center positions of the four embedded targets were determined to be (-1.5 mm, -5.35 mm), (-1.5 mm, -6.15 mm), (-0.7 mm, -5.35 mm), and (-0.7 mm, -6.15 mm) from the center of the phantom. We then performed an XLCT scan of the phantom to validate the proposed method as seen in Fig. 5. We operated the x-ray tube at 30 kV and 0.5 mA and took measurements at 6 projections (30º/projection) using 520 steps of 50 μm step size (four times smaller step size than our normal parameters). Lastly, we acquired 10 milliseconds of data from the PMT at each step, similar to [12].

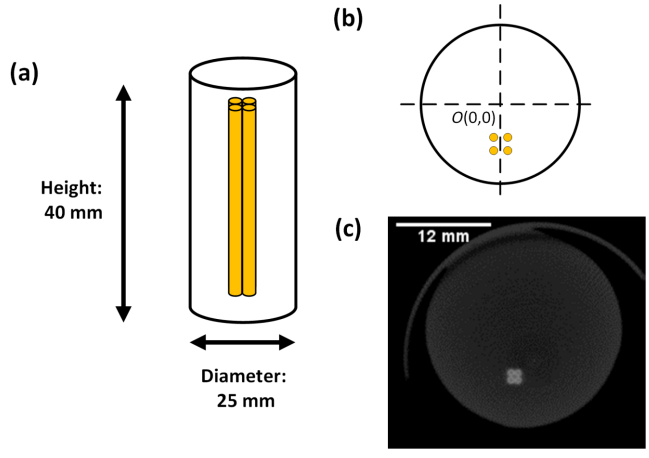

Fig. 4. Phantom for experimental studies. (a) Schematic side-view; (b) Schematic top-view; (c) microCT image of phantom used in study.

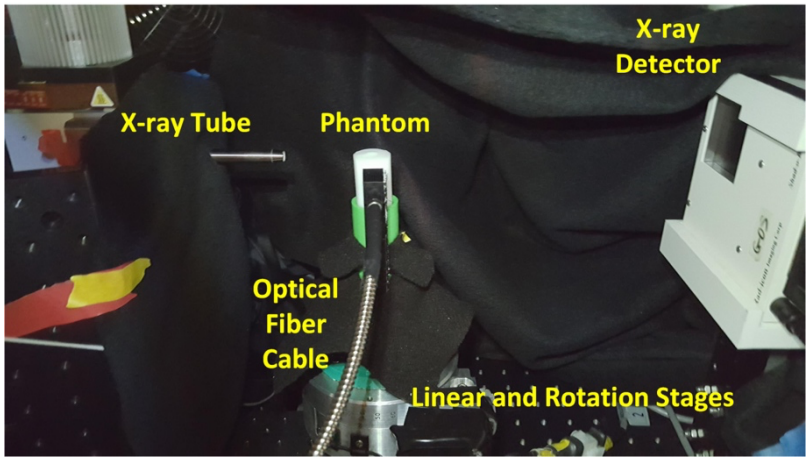

Fig. 5. Phantom set-up inside of XLCT system.

E. XLCT Image Quality Evaluation Criteria

To analyze the reconstructed XLCT images quantitatively, four criteria were used to evaluate the quality of the reconstructed XLCT images:

1) Dice Similarity Coefficient (DICE) [24]: DICE is used for quantifying the shape and location accuracy between the reconstructed and true target regions, which is obtained as follows:

$$DICE = \frac{2\times|\mathrm{ROI}_r \cap \mathrm{ROI}_t|}{|\mathrm{ROI}_r|+|\mathrm{ROI}_t|}\times 100\% \quad (1)$$

where ROI_r is the reconstructed region of interest that is defined to be the pixels whose intensities are higher than 10% of the maximum of the normalized reconstructed intensity, and ROI_t is the true target locations. Generally, closer the DICE is to 100%, the better the reconstruction accuracy.

2) Target Size Error (TSE) [8]: This criterion is defined as the target diameter error ratio between the reconstructed target and the true target:

$$TSE = \frac{|D_r - D_t|}{D_t} \times 100\% \tag{2}$$

where D_r and D_t is the diameter of reconstructed and true target, respectively. D_r is calculated from the cross target profile plot by using the full width tenth maximum (FWTM) approach, in which we measured the width at the tenth of the maximum.

3) Spatial Resolution Index (SPI) [25]: SPI is used to evaluate the performance of our proposed scanning strategy in resolving two targets and is calculated as:

$$SPI = \frac{\rho^l_{\max} - \rho^l_{valley}}{\rho^l_{\max} - \rho^l_{\min}} \tag{3}$$

where ρ^l denotes the value of the profile along a given line on the reconstructed cross-section. $\rho^l_{\max}$, $\rho^l_{\min}$ and ρ^l_{valley} are the maximal, minimal and valley value between the two peak values, respectively. The closer SPI is to 1, the better in resolving adjacent targets.

4) The Normalized Mean Square Error (NMSE) [26]: NMSE is applied to evaluate the relative error between the reconstructed and true targets, which is defined as

$$NMSE = \frac{\| \hat{\boldsymbol{\rho}} - \boldsymbol{\rho} \|_2^2}{\| \boldsymbol{\rho} \|_2^2} \quad (4)$$

where $\hat{\boldsymbol{\rho}}$ and $\boldsymbol{\rho}$ are the reconstructed and actual nanophosphor distributions, respectively.

III. RESULTS

A. Numerical simulations

XLCT image reconstruction was performed using the L^1 regularization method with the Majorization-Minimization (MM) reconstruction framework, developed in [16] but adapted to solve the inverse problem in XLCT imaging, following the steps as described in [23, 24, 27]. For the XLCT simulations, the phantom was discretized by a finite-element mesh (FEM) with 26,638 nodes, 153,053 tetrahedral elements, and 11,456 face elements and the reconstructed section was interpolated onto a grid of 25×25 μm^2 pixel size and then the system matrix was interpolated onto the grid from the FEM.

For the simulations of Phantom A, we simulated XLCT scanning using a straight x-ray beam with a fixed diameter of 0.8 mm but with different scanning step sizes from 0.8, 0.4, 0.2 to 0.1 mm. Fig. 6 plots the reconstructed XLCT images of Phantom A with different scanning beam sizes of 0.8 mm (Fig. 6a), 0.4 mm (Fig. 6b), 0.2 mm (Fig. 6c), and 0.1 mm (Fig. 6d). From Fig. 6, we can see substantial improvements in the image quality by decreasing the scanning step size. Figure 6(e) shows intensity profiles along the center line of the middle row targets in Figs. 6(a)-(d). The quantitative analysis results of the simulations using Phantom A are presented in Table II. As shown in Table II, when the scanning step size reduces from 0.8 to 0.1 mm, each of the calculated image quality metrics improved quite substantially. This indicates the improvements in shape and location accuracy, target size accuracy, spatial

resolution and overall reconstruction accuracy. There is a further increment of DICE and decrement of TSE and NMSE as the scanning step size decreases from 0.4 to 0.2 mm. There are no significant changes in DICE, TSE, SPI and NMSE when the scanning step size is reduced from 0.2 (Fig. 6(c)) to 0.1 mm (Fig. 6(d)).

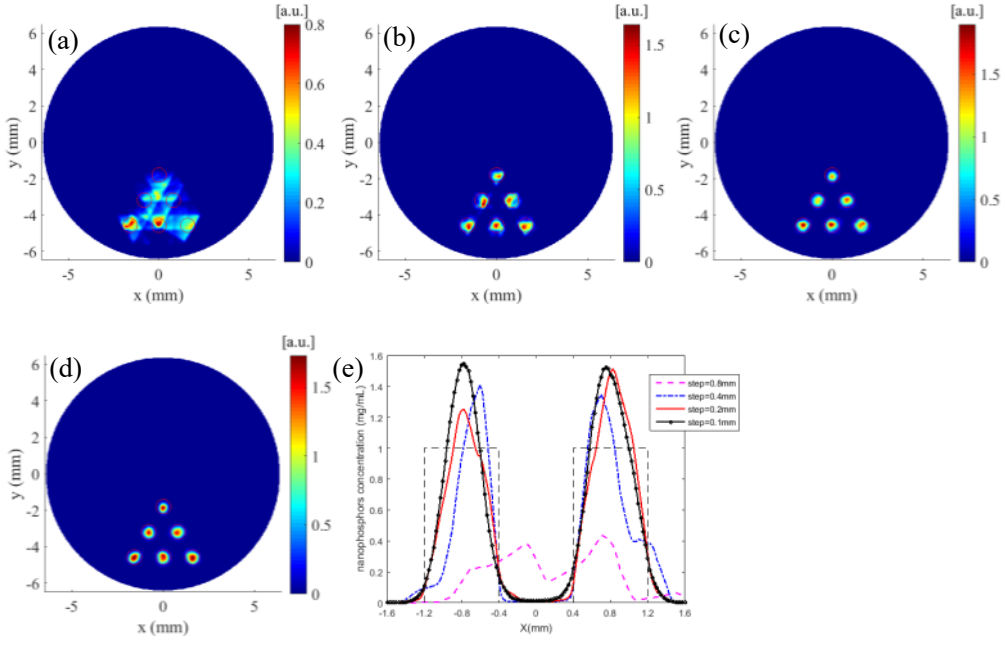

Fig. 6. Reconstructed XLCT images for the simulations of Phantom A with different scanning step sizes: (a) 0.8 mm, (b) 0.4 mm, (c) 0.2 mm and (d) 0.1 mm. (e) Intensity profiles along the center line of the middle row targets of Phantom A.

Table II.
THE QUANTITATIVE METRICS FOR THE SIMULATIONS OF PHANTOM A WITH DIFFERENT SCANNING STEP SIZES

Scan step (mm)	DICE (%)	TSE (%)	SPI	NMSE
0.8	39.7079	38.80	0.6929	0.6018
0.4	83.5759	10.94	0.9941	0.1907
0.2	90.7133	4.95	0.9951	0.1394
0.1	90.6076	6.25	0.9921	0.1317

For the simulations of Phantom B, we simulated XLCT scanning with the same scan settings as the previous simulation. Figure 7 shows the

reconstruction images of Phantom B. The six targets were hardly resolved when the scanning step size of 0.8 mm was adopted as shown in Fig. 7(a). When the scanning step size of 0.4 mm which is smaller than the target diameter was used, the six targets were easily resolved with better shapes at the correct locations as shown in Fig. 7(b). The quality of the reconstructed images were improved further by decreasing the scanning step size to 0.2 and 0.1 mm, as shown in Figs. 7(c) and (d). Figure 7(e) plots the intensity profiles along the center line of the middle row targets in Figs. 7(a)-(d). The quantitative analysis results are listed in Table III, from which we see the improvement of the reconstruction quality such as the shape and location accuracy, target size accuracy, spatial resolution and reconstruction accuracy when the scanning beam size was reduced. We have also noticed that there are only slight differences in the quantitative analysis results of DICE, SPI and NMSE when the scanning step size reducing from 0.2 to 0.1 mm.

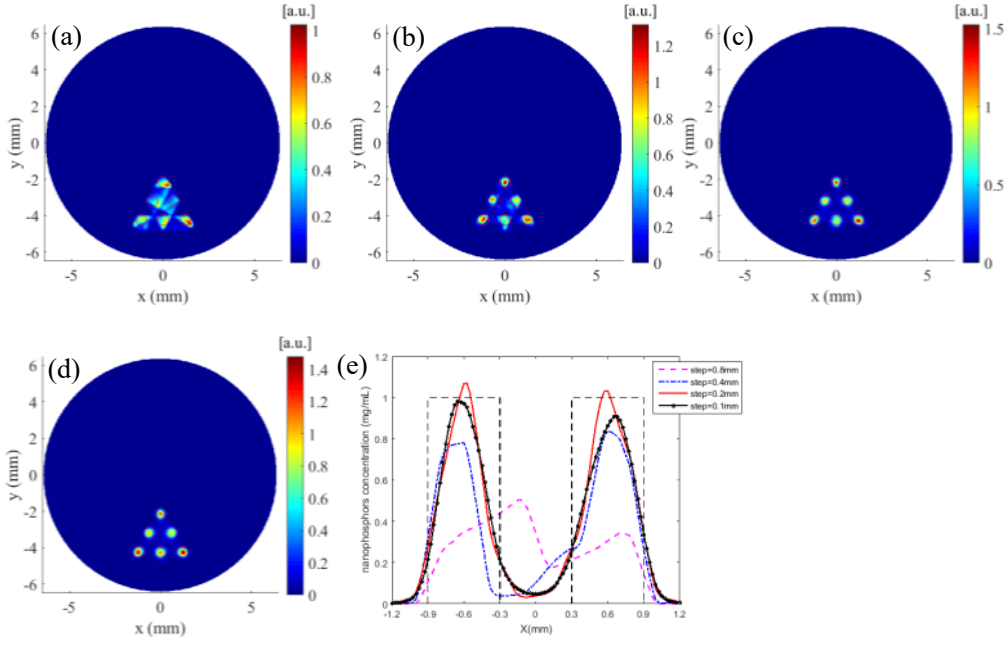

Fig. 7. Reconstructed XLCT images for the simulations of Phantom B with different scanning step sizes: (a) 0.8 mm, (b) 0.4 mm, (c) 0.2 mm and (d) 0.1 mm. (e) Intensity profiles along the center line of the middle row targets of Phantom B.

Table III.
THE QUANTITATIVE METRICS FOR THE SIMULATIONS OF PHANTOM B WITH DIFFERENT SCANNING STEP SIZES

Scan step (mm)	DICE (%)	TSE (%)	SPI	NMSE
0.8	55.9029	32.99	0.6485	0.4850
0.4	70.3355	22.92	0.9542	0.2264
0.2	81.7327	17.71	0.9701	0.1594
0.1	80.9331	12.85	0.9515	0.1635

We have conducted numerical simulations on Phantom C with the same scan settings as the previous simulations. The reconstructed images of Phantom C are plotted in Fig. 8, from which we can see that all targets could be resolved successfully for the step sizes of 0.2 and 0.1 mm. Intensity profiles along the center line of the middle row targets in Figs. 8(a)-(d) were drawn and displayed in Fig. 8(e). The DICE, TSE, SPI and NMSE of the reconstruction results were calculated and are listed in Table IV. As the scanning step size reduced from 0.8 to 0.1 mm, the SPI increased monotonically from 0.8358 to 0.9245, indicating that the proposed scanning strategy with a smaller scanning step size achieved much better separation of the targets. At the same time, a monotonic improvement of the reconstruction accuracy can be maintained as indicated by the NMSE shown in Table IV. The reduction of scanning step size can result in better accuracy of the reconstructed shape and location of targets as indicated by the DICE and the TSE.

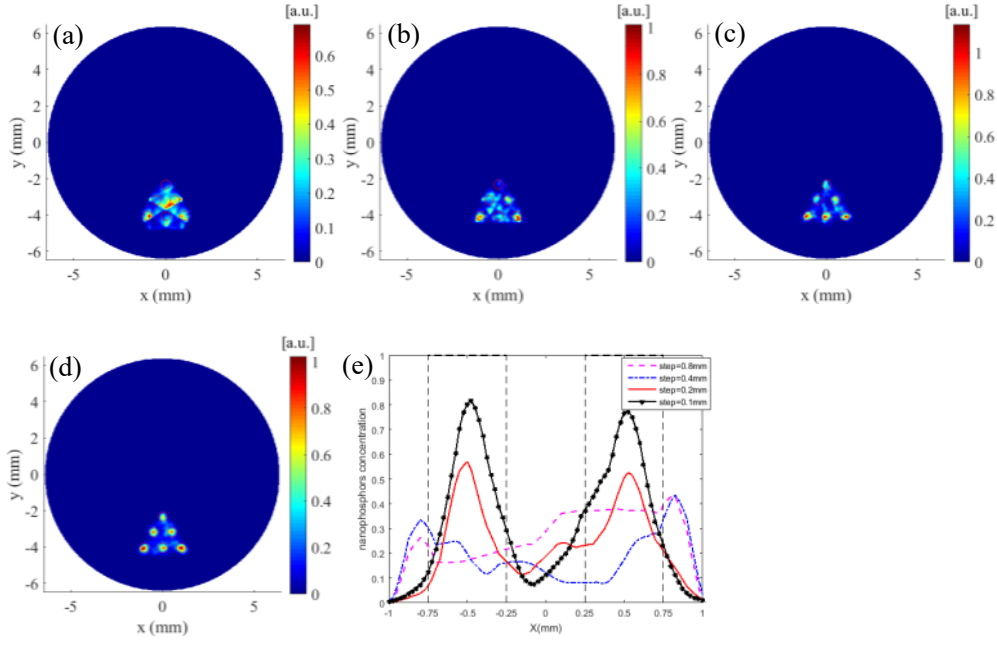

Fig. 8. Reconstructed XLCT images for the simulations of Phantom C with different scanning step sizes: (a) 0.8 mm, (b) 0.4 mm, (c) 0.2 mm and (d) 0.1 mm. (e) Intensity profiles along the center line of the middle row targets of Phantom C.

Table IV
THE QUANTITATIVE METRICS FOR THE SIMULATIONS OF PHANTOM C WITH DIFFERENT SCANNING STEP SIZES

Scan step (mm)	DICE (%)	TSE (%)	SPI	NMSE
0.8	38.8433	59.17	0.8358	0.7669
0.4	47.0148	45.42	0.8721	0.6012
0.2	58.5172	43.33	0.9044	0.4373
0.1	53.6614	36.25	0.9245	0.3320

To further study the performance limitation of the proposed scanning strategy in resolving targets with a diameter smaller than the x-ray beam width, we simulated XLCT imaging of Phantom D, in which both the target diameter and the EED were set to be 0.4 mm, half of the beam diameter. Figure 9 shows the reconstruction XLCT images for this case. From Fig. 9, we can see that image quality has improved slightly when the step size

decreased. However, the reconstructed XLCT image could not resolve all the six targets even if the step size is reduced to 0.1 mm.

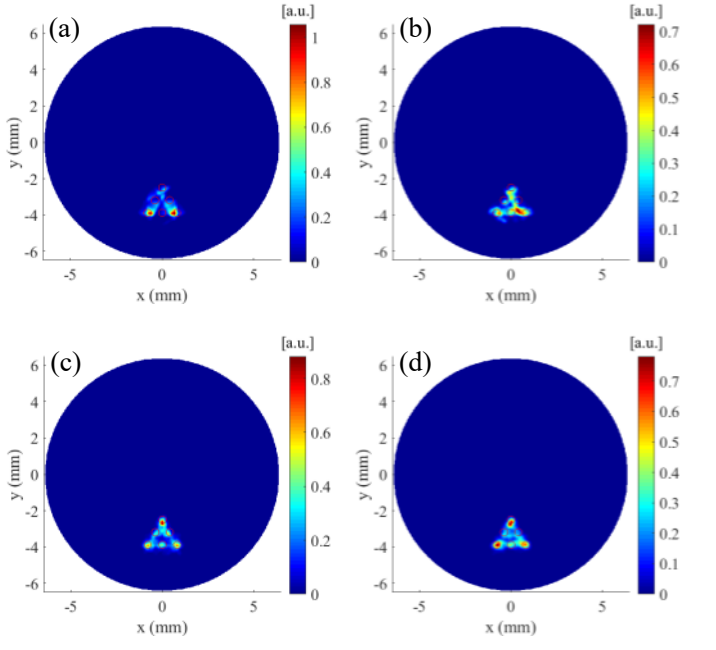

Fig. 9. Reconstructed XLCT images for the simulations of Phantom D with different scanning step sizes: (a) 0.8 mm, (b) 0.4 mm, (c) 0.2 mm and (d) 0.1 mm.

B. Phantom experiment

XLCT image reconstruction was performed from the measurements using a similar approach as the numerical simulations. The L^1 regularized MM algorithm was again utilized with the same FEM, interpolated onto a 50×50 μm^2 grid. From the XLCT measurement data, we reconstructed three different cases, differing by their linear scanning step sizes: 200 μm (no reduction in step size), 100 μm (two times reduction in step size), and 50 μm (four times reduction in step size) and plotted the results and their corresponding line profile plots for the respective cases in Figs. 10, 11, and 12. We also performed quantitative analyses by calculating the DICE, TSE and SPI as shown in Table V. The true target locations (ground truth) were determined from the microCT image (Fig. 4(c)) and are shown by the green circles in the

reconstructed XLCT images. Overall we can see that as the step size decreased, there was an overall improvement in the image quality and the ability to resolve the targets. In addition, the DICE increased from 50.7289 to 53.1746 and finally to 67.1642 %, the TSE decreased from 12.50 to 10.94, and finally to 7.81%, and the SPI has an obvious improvement from 0.7615 to 0.9061, and finally to 0.9221, as the step size decreased from 200, to 100, and finally to 50 μm (Table IV). Overall our XLCT image reconstruction successfully validates the improvement from our proposed scanning strategy.

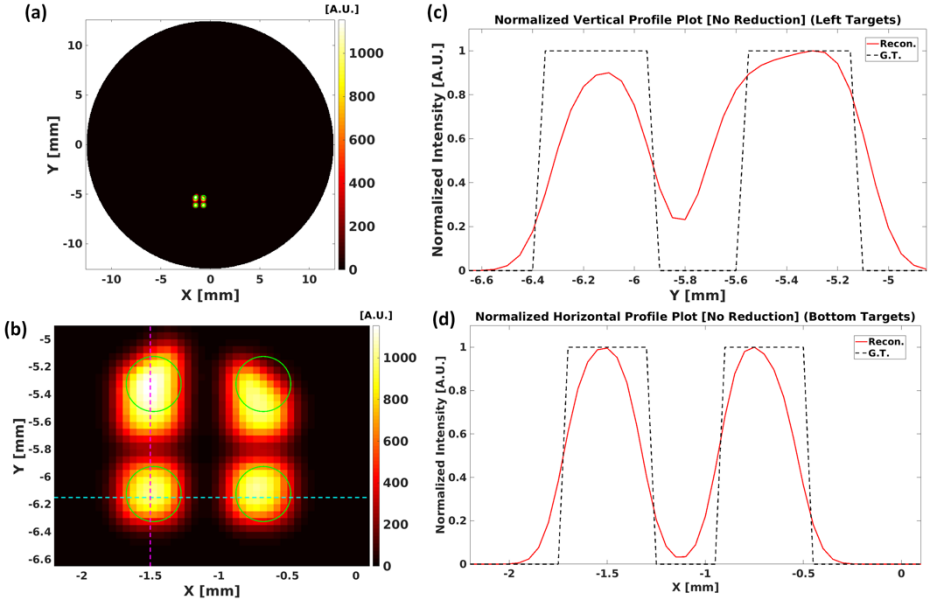

Fig. 10. XLCT reconstruction with no step size reduction.(200 μm step size). (a) Reconstructed XLCT image; (b) Zoomed-in target region. The green circles show the true target locations. (c) Normalized vertical line profile plot (magenta line); (d) Normalized horizontal line profile plot (blue line).

Fig. 11. XLCT reconstruction for 2x step size reduction (100 μm step size). (a) Reconstructed XLCT image; (b) Zoomed-in target region. The green circles show the true target locations. (c) Normalized vertical line profile plot (magenta line); (d) Normalized horizontal line profile plot (blue line).

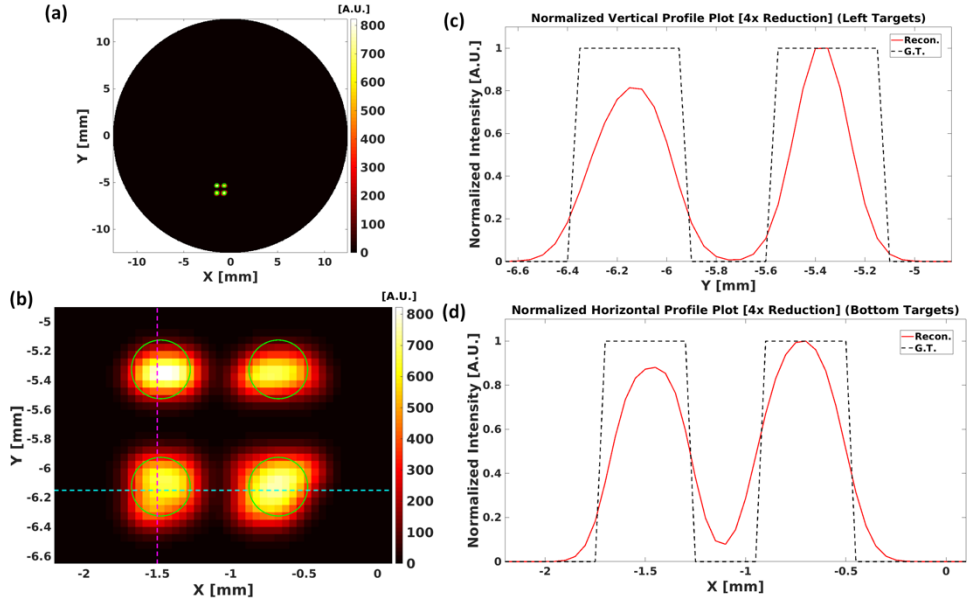

Fig. 12. XLCT reconstruction for 4x step size reduction (50 μm step size). (a) Reconstructed XLCT image; (b) Zoomed-in target region. The green circles show the true target locations. (c) Normalized vertical line profile plot (magenta line); (d) Normalized horizontal line profile plot (blue line).

Table V

Image Quality Metrics of XLCT reconstructed images for the phantom experiment.

Case	DICE (%) (FWHM) [Bottom Targets]	TSE (%) (FWHM)	SPI
No Step Reduction (step size of 200 μm)	50.7289	12.50	0.7615
2x Step Size Reduction (step size of 100 μm)	53.1746	10.94	0.9061
4x Step Size Reduction (step size of 50 μm)	67.1642	7.81	0.9221

IV. DISCUSSION AND CONCLUSION

State-of-the-art high-resolution imaging techniques are a driving force behind current biomedical science. Among such, microscopic XLCT imaging stands out as it has the potentials to obtain both high sensitivity and spatial resolution. However, its high spatial resolution capacity has not been fully implemented yet. According to previous studies, the spatial resolution limit of XLCT is

generally believed to be determined by the beam aperture size. Therefore，generation of super fine x-ray beams, such as super fine collimated x-ray beams imaging [11] and focused x-ray beams imaging [12], is generally thought to be the only way to improve the spatial resolution of XLCT imaging. However, both methods for generating superfine beams each has their own shortcomings. In this paper, a new scanning strategy, in which the scanning step size is reduced to be less than the x-ray beam size, is proposed to break the spatial resolution limit of the traditional narrow x-ray beam based XLCT system.

The numerical simulations have demonstrated that the proposed scanning strategy of a smaller step size can achieve better results in the DICE, TSE and SPI than the traditional one where the step size was equal to the x-ray beam diameter. We have found that targets can be resolved successfully with the proposed scanning strategy when the target size and the EED between targets are smaller than the beam width. We also conducted XLCT scanning simulations on phantoms with smaller EED (e.g. target size = 0.6 mm, EED = 0.4mm). Under these circumstances, the proposed scanning strategy can also improve the reconstruction quality for resolving the six targets. These results are not included in this paper for simplicity. These findings extend the theory that the spatial resolution of XLCT is not only determined by the beam size but also the scanning step size The numerical simulations have demonstrated that our proposed method was stable and robust against noises. The experimental results of phantom have further validated that the proposed scanning strategy can achieve better results in XLCT reconstruction.

Certainly, there is an upper bound of spatial resolution improvement by reducing the scanning step size, which will be further studied in the future. We have shown that XLCT imaging with reduced scanning step size can

reach a better spatial resolution. However, the reduced step size based scanning strategy needs more scan steps to cover the same field of view as before, which means more measurement time is required with the current configuration. To overcome this problem of long scanning time, we used a highly sensitive PMT and a focused x-ray beam with high x-ray intensity to reduce the measurement time per scan step. The current measurement time with the step size of 50 μm was 6×520×10 milliseconds or 31.2 seconds if neglecting the stage movement time. The measurement time can be further reduced to make it more suitable for practical use. One possible way is incorporation of the pre-acquired permissible region of the targets into the scanning configuration to reduce the scanning area and improve the scanning efficiency. The permissible region strategy has been adopted in a cone beam based XLCT imaging [14].

In the previous work, we have performed sensitivity study of XLCT [28] under the traditional scanning strategy. In this study, we do not expect the sensitivity to be reduced because other imaging parameters were kept the same as before except the reduced scanning step size. The sensitivity study of the proposed approach should be studied further in the future.

In sum, we have performed four sets of numerical simulations and one set of phantom experiments to validate the proposed new scanning scheme of XLCT imaging. Our results have demonstrated that the new scanning scheme can improve the spatial resolution substantially. In particular, the improvement is up to 2 times from 0.8 mm to 0.4 mm for the case with an x-ray beam diameter of 0.8 mm.

Disclosures

The authors declare that there are no conflicts of interest related to this article.

Acknowledgments

The authors acknowledge the funding supports from the National Natural Science Foundation of China (81571723) and the National Institutes of Health (NIH) [R01 EB026646]. The authors also acknowledge Dr. Simon R. Cherry from UC Davis for lending us the microCT system used in this study.

REFERENCES

[1] C. M. Carpenter, C. Sun, G. Pratx, R. Rao, and L. Xing, "Hybrid x-ray/optical luminescence imaging: characterization of experimental conditions," *Med. Phys.,* vol. 37, pp. 4011-8, 2010.

[2] G. Pratx, C. M. Carpenter, C. Sun, R. P. Rao, and L. Xing, "Tomographic molecular imaging of x-ray-excitable nanoparticles," *Opt. Lett.,* vol. 35, pp. 3345-7, 2010.

[3] G. Pratx, C. M. Carpenter, C. Sun, and L. Xing, "X-ray luminescence computed tomography via selective excitation: a feasibility study," *IEEE Trans. Med. Imag.,* vol. 29, pp. 1992-9, 2010.

[4] C. Li, G. Wang, J. Qi, and S. R. Cherry, "Three-dimensional fluorescence optical tomography in small-animal imaging using simultaneous positron-emission-tomography priors," *Opt. Lett.,* vol. 34, pp. 2933-5, 2009.

[5] W. Cong, C. Wang, and G. Wang, "Stored luminescence computed tomography," *Appl. Opt.,* vol. 53, pp. 5672-6, 2014.

[6] W. Zhang, D. Zhu, K. Zhang, and C. Li, "Microscopic x-ray luminescence computed tomography," *Proc. SPIE,* vol. 9316, p. 93160M, 2015.

[7] S. Tzoumas, D. Vernekohl, and L. Xing, "Coded-Aperture Compressed Sensing X-Ray Luminescence Tomography," *IEEE Trans. Biomed. Eng.,* vol. 65, pp. 1892-1895, 2016.

[8] W. Zhang, D. Zhu, M. Lun, and C. Li, "Multiple pinhole collimator based X-ray luminescence computed tomography," *Biomed. Opt. Express,* vol. 7, pp. 2506-23, 2016.

[9] G. Zhang, F. Liu, J. Liu, J. Luo, Y. Xie, J. Bai*, et al.*, "Cone Beam X-ray Luminescence Computed Tomography Based on Bayesian Method," *IEEE Trans. Med. Imag.,* vol. 36, pp. 225-235, 2017.

[10] W. Zhang, M. C. Lun, A. A. Nguyen, and C. Li, "X-ray luminescence computed tomography using a focused x-ray beam," *J. Biomed. Opt.,* vol. 22, pp. 1-11, 2017.

[11] W. Zhang, D. Zhu, M. Lun, and C. Li, "Collimated superfine x-ray beam based x-ray luminescence computed tomography," *J. Xray Sci. Technol.,* vol. 25, pp. 945-957, 2017.

[12] M. C. Lun, W. Zhang and C. Li, "Focused x-ray luminescence computed tomography: experimental studies," *Proc. of SPIE,* vol. 10871, p.108710G , 2019.

[13] W. Cong, H. Shen, and G. Wang, "Spectrally resolving and scattering-compensated x-ray luminescence/fluorescence computed tomography," *J. Biomed. Opt.,* vol. 16, p. 066014, 2011.

[14] H. Yi, X. Qu, Y. Sun, J. Peng, Y. Hou, and X. He, (2017, Dec). "A permissible region extraction based on a knowledge priori for X-ray luminescence computed tomography" [Online]. *Multimedia Systems*. Available: https://doi.org/10.1007/s00530-017-0576-3.

[15] G. Zhang, S. Tzoumas, K. Cheng, F. Liu, J. Liu, J. Luo*, et al.*, "Generalized Adaptive Gaussian Markov Random Field for X-Ray Luminescence Computed Tomography," *IEEE Trans. Biomed. Eng.,* vol. 65, pp. 2130-2133, 2018.

[16] Y. Tian, W.-H. Cao, X.-X. Luo, and Y. Fu, "Preparation and luminescence property of Gd2O2S:Tb X-ray nano-phosphors using the complex precipitation method," *Journ. of All. and Comp.* vol. 433, pp. 313-317, 2007.

[17] Y. Osakada, G. Pratx, L. Hanson, P. E. Solomon, L. Xing, and B. Cui, "X-ray excitable luminescent polymer dots doped with an iridium(III) complex," *Chem. Commun .(Camb.),* vol. 49, pp. 4319-21, 2013.

[18] L. Sudheendra, G. K. Das, C. Li, D. Stark, J. Cena, S. Cherry*, et al.*, "NaGdF4:Eu(3+) Nanoparticles for Enhanced X-ray Excited Optical Imaging," *Chem. Mater.,* vol. 26, pp. 1881-1888, 2014.

[19] W. Zhang, Y. Shen, M. Liu, P. Gao, H. Pu, L. Fan*, et al.*, "Sub-10 nm Water-Dispersible beta-NaGdF4:X% Eu(3+) Nanoparticles with Enhanced Biocompatibility for in Vivo X-ray Luminescence Computed Tomography," *ACS Appl. Mater. Interfaces,* vol. 9, pp. 39985-39993, 2017.

[20] T. Guo, Y. Lin, W. J. Zhang, J. S. Hong, R. H. Lin, X. P. Wu*, et al.*, "High-efficiency X-ray luminescence in Eu(3+)-activated tungstate nanoprobes for optical imaging through energy transfer sensitization," *Nano.,* vol. 10, pp. 1607-1612, 2018.

[21] D. Chen, S. Zhu, H. Yi, X. Zhang, D. Chen, J. Liang*, et al.*, "Cone beam x-ray luminescence computed tomography: a feasibility study," *Med. Phys.,* vol. 40, p. 031111, 2013.

[22] D. Chen, S. Zhu, X. Chen, T. Chao, X. Cao, F. Zhao*, et al.*, "Quantitative cone beam X-ray luminescence tomography/X-ray computed tomography imaging," *Appl. Phys. Lett.,* vol. 105, p. 191104, 2014.

[23] C. Li, A. Martinez-Davalos, and S. R. Cherry, "Numerical simulation of x-ray luminescence optical tomography for small-animal imaging," *J. Biomed. Opt.,* vol. 19, p. 046002, 2014.

[24] D. Zhu and C. Li, "Nonconvex regularizations in fluorescence molecular tomography for sparsity enhancement," *Phys. Med. Biol.,* vol. 59, pp. 2901-12, Jun 21 2014.

[25] P. Gao, J. Rong, H. Pu, T. Liu, W. Zhang, X. Zhang*, et al.*, "Sparse view cone beam X-ray luminescence tomography based on truncated singular value decomposition," *Opt. Expr.,* vol. 26, pp. 23233-23250, 2018.

[26] D. Chen, S. Zhu, X. Cao, F. Zhao, and J. Liang, "X-ray luminescence computed tomography imaging based on X-ray distribution model and adaptively split Bregman method," *Biomed. Opt. Expr.,* vol. 6, pp. 2649-63, 2015.

[27] D. Zhu and C. Li, "Nonuniform update for sparse target recovery in fluorescence molecular tomography accelerated by ordered subsets," *Biomed. Opt. Express,* vol. 5, pp. 4249-59, 2014.

[28] M. C. Lun, W. Zhang, and C. Li, "Sensitivity study of x-ray luminescence computed tomography," *Appl. Opt.,* vol. 56, pp. 3010-3019, 2017.

[29] C. T. Badea, I. N. Stanton, S. M. Johnston, G. A. Johnson, and M. J. Therien, "Investigations on X-ray luminescence CT for small animal imaging," *Proc. of SPIE.,* vol. 8313, p. 83130T, 2012.